ACS NANO
Cite This: ACS Nano 2018, 12, 3487−3501
www.acsnano.org
ARTICLE

Toward Self-Control Systems for Neurogenic Underactive Bladder: A Triboelectric Nanogenerator Sensor Integrated with a Bistable Micro-Actuator

Faezeh Arab Hassani,*[†,‡,§] Roshini P. Mogan,[‡] Gil G. L. Gammad,[‡] Hao Wang,[†,‡,§,∥] Shih-Cheng Yen,*[†,‡] Nitish V. Thakor,*[†,‡] and Chengkuo Lee*[†,‡,§,∥,⊥]

[†]Department of Electrical and Computer Engineering, Faculty of Engineering, National University of Singapore, 4 Engineering Drive 3, #05-45, Singapore 117583, Singapore

[‡]Singapore Institute for Neurotechnology, National University of Singapore, 28 Medical Drive, #05-COR, Singapore 117456, Singapore

[§]Center for Intelligent Sensors and MEMS, National University of Singapore, 5 Engineering Drive 1, E6 #05-11F, Singapore 117608, Singapore

[∥]Hybrid-Integrated Flexible Electronic Systems (HIFES) Program, National University of Singapore, 5 Engineering Drive 1, E6 #05-4, Singapore 117608, Singapore

[⊥]NUS Graduate School for Integrative Science and Engineering, National University of Singapore, Singapore 117456, Singapore

S *Supporting Information*

ABSTRACT: **Aging, neurologic diseases, and diabetes are a few risk factors that may lead to underactive bladder (UAB) syndrome. Despite all of the serious consequences of UAB, current solutions, the most common being ureteric catheterization, are all accompanied by serious shortcomings. The necessity of multiple catheterizations per day for a physically able patient not only reduces the quality of life with constant discomfort and pain but also can end up causing serious complications. Here, we present a bistable actuator to empty the bladder by incorporating shape memory alloy components integrated on flexible polyvinyl chloride sheets. The introduction of two compression and restoration phases for the actuator allows for repeated actuation for a more complete voiding of the bladder. The proposed actuator exhibits one of the highest reported voiding percentages of up to 78% of the bladder volume in an anesthetized rat after only 20 s of actuation. This amount of voiding is comparable to the common catheterization method, and its one time implantation onto the bladder rectifies the drawbacks of multiple catheterizations per day. Furthermore, the scaling of the device for animal models larger than rats can be easily achieved by adjusting the number of nitinol springs. For neurogenic UAB patients with degraded nerve function as well as degenerated detrusor muscle, we integrate a flexible triboelectric nanogenerator sensor with the actuator to detect the fullness of the bladder. The sensitivity of this sensor to the filling status of the bladder shows its capability for defining a self-control system in the future that would allow autonomous micturition.**

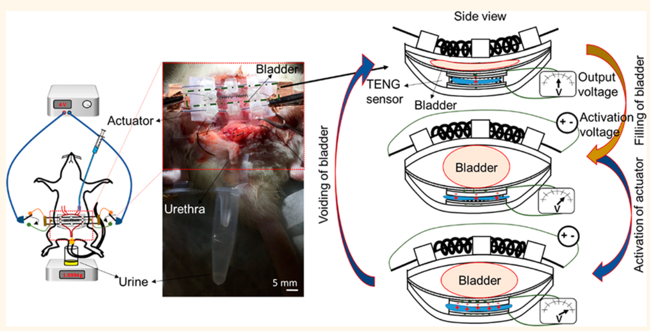

KEYWORDS: *shape memory alloy actuator, flexible, bistable, restoration−compression, triboelectric nanogenerator sensor, myogenic and neurogenic underactive bladder*

Rapid progress in the advancement of wearable medical electronics with the help of flexible materials eases the continuous monitoring and evaluation of vital biological signals from the body.[1,2] For instance, flexible electronic skins can sense pressure,[3] while wearable patches are capable of measuring temperature, hydration, blood pressure and oxygen level, biomarkers in sweat, and electrophysiology signals.[4−7] Numerous implantable devices have been also designed based

Received: January 12, 2018
Accepted: April 9, 2018
Published: April 9, 2018

DOI: 10.1021/acsnano.8b00303
ACS Nano 2018, 12, 3487−3501

on biocompatible, soft, and stretchable materials for diagnostic and therapeutic applications.[1,2,8] Direct attachment of an electrode array on an organ surface such as brain or heart can be used to record electrophysiological signals and produce a high-resolution map of the physiological signals.[9−11] Flexible neural electrodes that can wrap around the nerves for recording and stimulating the activity of the nervous system are additional examples of implantable devices.[12]

The material compatibility and shape memory property of shape memory alloy (SMA) materials such as nitinol (NiTi) makes them liable for fabricating implantable biomedical devices.[13−17] The shape memory property of the SMA materials is due to atomic-level structural changes in the material from the martensitic to the austenite phase by applying heat.[18] The molecular structure in the martensitic phase is twinned.[19] Due to the heating (through the austenite start temperature, A_S, and finish austenite temperature, A_F), the atoms in the crystal rearrange into a cubic arrangement called the austenite phase. The reverse transformation on cooling (through the martensitic start temperature, M_S, and finish martensitic temperature, M_F) brings back the crystal structure to the martensitic phase.[18−21] Such structural changes in the material happen at the transition temperature that is defined in the original thermal training of the material.[18−21] Stents, super elastic wires for laparoscopic surgery, clips for the control of gastrointestinal bleeding, staples, and clamps for orthopedic surgery are a few biomedical applications of SMA-based devices.[22] One area of particular clinical need and applicability is to develop actuators to help with the voiding of the under active bladder (UAB).

UAB is a complex condition that dramatically affects a patient's life.[23,24] UAB defines a group of symptoms including prolonged/failed bladder emptying within a normal time span.[25] UAB is closely related to detrusor underactivity and may be initiated by aging, neurological disorders and infections, and diabetes to name a few.[23−27] However, interventions for patients with this condition have not been explored as much compared to interventions for patients with overactive bladder (OAB).[26] Double voiding or straining the bladder to void, indwelling or intermittent catheterization, drug, stem/gene therapy, and sacral nerve stimulation are the current treatments.[27,28] Intermittent catheterization is the method of choice for UAB patients.[27,28] Even if the catheterization can relieve the bladder sufficiently, the necessity of multiple daily insertions may lead to complications such as urinary tract infection (UTI) and asymptomatic bacteriuria (ASB).[29−31]

Previous works[32,33] have demonstrated SMA-based actuators in the form of parallel and interlaced devices, consisting of SMA wires and 3D printed vests, were used for the voiding of the bladder. The focus of the previously proposed actuators was on the configuration and anchorage of SMA wires onto the flexible vests. However, the current work proposes a simple but effective mechanism with the help of a NiTi spring and flexible sheets for voiding of the bladder. Furthermore, voiding efficacy for the previous actuators was not sufficient to be practical: A maximum voiding percentage of only 23.59% was achieved in an anesthetized rat model due to the conformability limitations of the vest. Moreover, for those actuators, the size of the vest should be matched with the bladder size; otherwise, the maximum voiding percentage reduced further. Any urine in the bladder after the device actuation due to incomplete voiding increased the risk of UTI. Incomplete emptying of the bladder with an approximate post-void residual urine volume (PVR) of more than 150 mL (with an initial bladder volume of about 500 mL)[34,35] is considered as chronic urinary retention and may result in the increased occurrence of UTI.[36−38] Since the contraction of the bladder in these actuators mainly depended on the 5% shortening of the SMA wires, the amount of compression force exerted was not large enough. For this reason, here we propose a design for the actuator by using a prestretched NiTi spring to greatly increase the compression force required for a more complete voiding of the bladder. Bistable actuation can also further increase the force exerted by the actuator.[39] In this work, we propose a mechanism that incorporates the large contraction force of a NiTi spring to achieve the bistable performance for doubly clamped flexible polyvinyl chloride (PVC) sheets. Such a mechanism magnifies the contraction force while keeping the applied voltage at the same level and lowering the power consumption of the previously reported actuators. Based on the size of the bladder, or due to the bladder wall thickening,[40] it may be necessary to actuate the NiTi spring multiple times for a complete voiding of the bladder. To achieve this criterion, a restoration phase is also added to the compression phase of the actuator with the help of two thick SMA wires. The compression−restoration capability of the actuator promotes the development of a design that can be fitted to a wide range of bladder sizes. In addition, the benefit of our approach is the biocompatibility of NiTi components[20] and PVC sheets,[41] and thus our approach can be applied for future clinical applications of this actuator.

The stretch receptors in a healthy bladder wall sense the bladder fullness, and the voiding initiated following the fullness of bladder.[42] Even though myogenic UAB patients experience incomplete voiding of the bladder due to the dysfunctional detrusor muscle, stretch receptors in their bladder wall are intact.[42] Therefore, the proposed actuator is sufficient to resolve the incomplete voiding. However, neurogenic UAB patients may suffer from a faulty nervous system as well as dysfunctional detrusor muscle that leaves them unable to detect the bladder fullness.[42] Therefore, a sensor can be used to determine the liquid volume in the bladder.

The implantable devices are modulated by an external power source such as batteries. However, harvesting biomechanical energy of body can resolve the necessity of this additional power source.[43,44] Realization of self-powered implantable devices may be possible by using triboelectric nanogenerators (TENGs) that are capable of producing a sufficient high-power output.[45−48] Previously implantable TENGs as nano energy sources for sensors have been explored by various research groups.[45,46,49] However, in this work, we integrated a sponge-based TENG as the sensing component with our actuator for detecting the fullness status of the bladder for the consequent activation of the actuator.

We present an actuator with a repeatable high voiding efficacy by using a compression and restoration mechanism, lower power consumption compared to the previously reported actuators, and scalable solution for larger sizes of bladder. We first present the actuation mechanism design including the compression and restoration phases and fabrication of the actuator for myogenic UAB. We tested the proposed actuator by using an experimental setup on a balloon. This was followed by an *in vivo* test of the actuator in an animal model. The TENG sensor was then designed and integrated with the actuator for neurogenic UAB and was tested in a successful *in vivo* experimental demonstration.

DOI: 10.1021/acsnano.8b00303
ACS Nano 2018, 12, 3487−3501

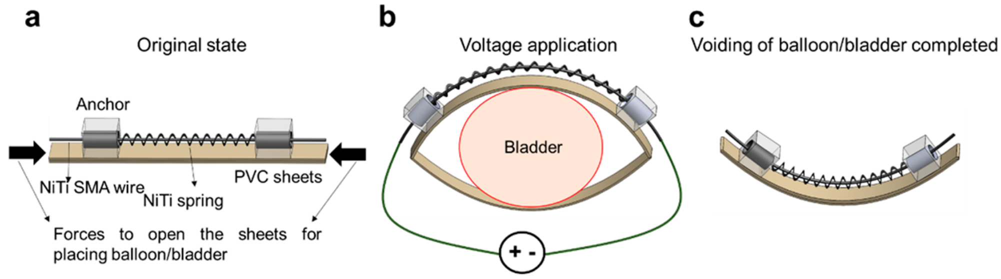

Figure 1. NiTi spring actuator and the actuation mechanism. (a) The actuator before placing the balloon or bladder, and the applied forces required for opening the PVC sheets. (b) The placement of balloon or bladder between the PVC sheets, and the application of voltage to the NiTi SMA wire. (c) The status of the spring actuator after the completion of voiding.

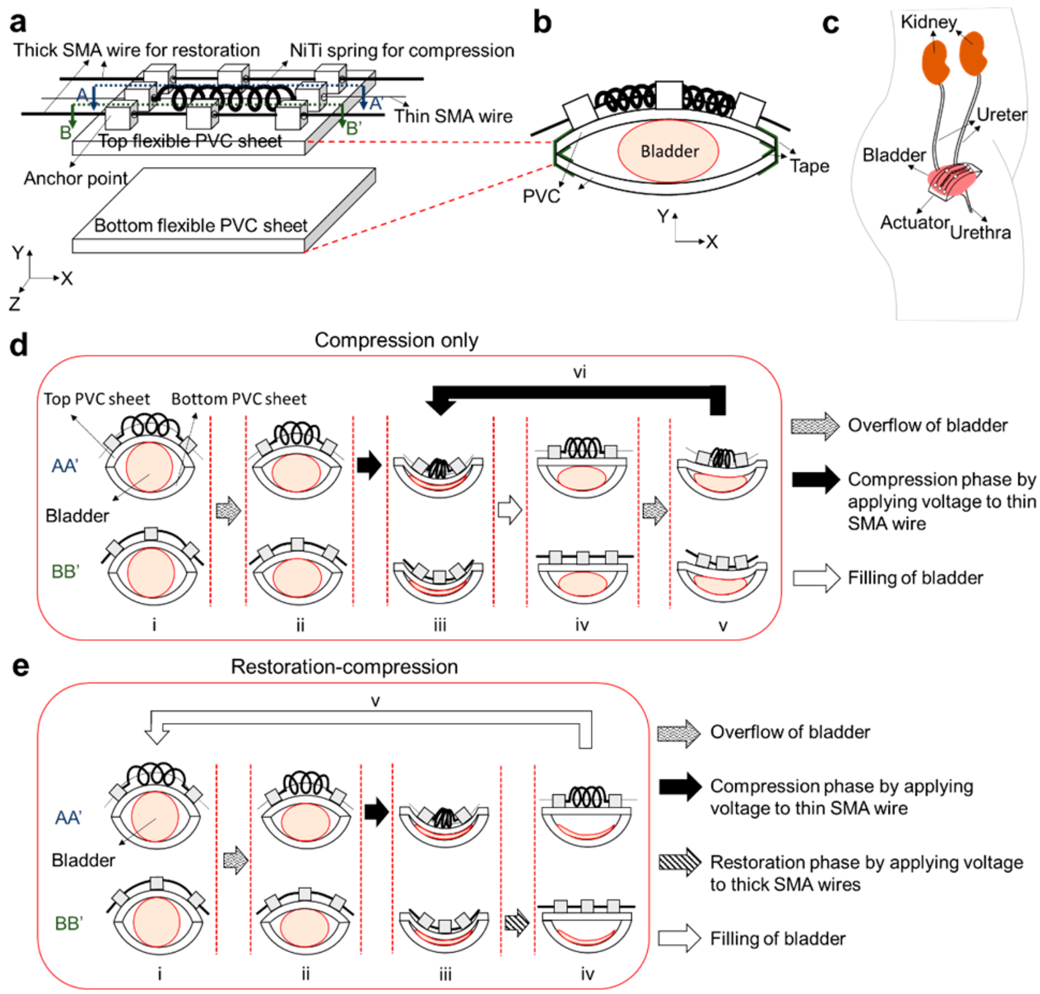

Figure 2. Compression and restoration phases for the NiTi spring actuator. (a) The schematic view of the disassembled parts of the NiTi spring actuator including the spring and thin SMA wire for the compression phase and thick SMA wires for the restoration phase. (b) The schematic side view of the assembled actuator. (c) The schematic application of the spring actuator on the bladder. (d) The schematic view of the operation of the actuator during the compression phase only. The cross section views are shown along the AA′ and BB′ dotted lines in (a). (e) The schematic view of the operation of the actuator while activating both restoration and compression phases. The cross section views are shown along the AA′ and BB′ dotted lines in (a).

RESULTS AND DISCUSSION

The NiTi Spring Actuation Mechanism. A 1 cm-length NiTi spring with a transition temperature of 45 °C,[50] outer body diameter, D_s, of 1.65 cm, total coils of 21, n_s, and wire diameter, d_s, of 250 μm was stretched up to the length of 2.4 cm, l_s, and then anchored by using two 3D printed anchor points onto a PVC sheet with the width, w, of 5 mm, length, l, of 5 cm, and thickness, h, of 400 μm. A thin SMA wire with the transition temperature of 70 °C and diameter of 200 μm[51] was passed through the spring. The SMA wire was heated by applying voltage that subsequently heated the spring up to 45 °C. The heating of the spring resulted in the reduction of its length, Δl_s. The assembled actuator is illustrated in Figure S1a. The plots of Δl_s *versus* time for various voltages of 3, 4, and 5 V are shown in Figure S1b. The Δl_s increased from 0 to 1.6 cm after 20 s of voltage application. By increasing the voltage from

DOI: 10.1021/acsnano.8b00303
ACS Nano 2018, 12, 3487−3501

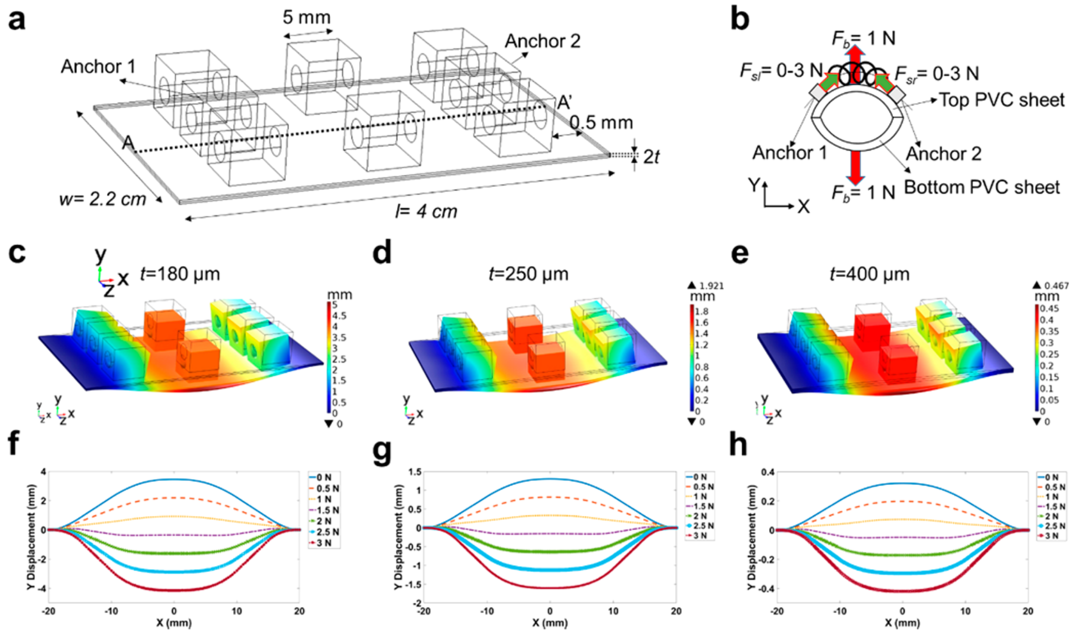

Figure 3. Numerical modeling of the NiTi spring actuator. (a) The schematic view of the NiTi spring actuator used for the numerical modeling. (b) The side view schematic of the forces applied to PVC sheets to define the force exerted by the balloon or bladder (F_b) and forces applied to anchors 1 and 2 to define the forces imposed by the spring ($F_{sl} = F_{sr}$). Actuators with various thicknesses of PVC sheets (*i.e.*, 180, 250, and 400 μm): (c−e) the out-of-plane displacement of the device at $F_{sl} = F_{sr} = 3$ N and (f−h) the side view plots of out-of-plane displacement along AA′ dotted line in (a).

3 to 5 V, Δl_s reached the maximum change of 1.6 cm much quicker. The spring started to contract after 1, 2, and 3 s of voltage application of 3, 4, and 5 V, respectively. In the subsequent experiments, 4 V was used as a compromise to avoid overheating of the SMA wire. Changes in the temperature of the SMA wire over time at 4 V voltage application is presented in Figure S1b. The wire temperature increased from 27.8 °C at $T = 0$ s to 65.2 °C at $T = 20$ s. Movie S1 presents the contraction of the actuator during 20 s of 4 V voltage application. A second PVC sheet with the same thickness and dimensions was attached along both the edges to the first PVC sheet by using common scotch tape (Figure 1a). By applying a slight force to the attached edges of PVC sheets, as shown in Figure 1a, a balloon or bladder can be placed between two PVC sheets (Figure 1b). A voltage was then applied to the thin SMA wire to heat and contract the spring. As a result of the spring contraction, the bending direction of PVC sheets changed from upward to downward, thus the balloon or bladder was compressed between the two PVC sheets (Figure 1c).

The Actuator Design and Fabrication. In order for the PVC sheets to completely cover the rubber balloon or bladder with the diameter of about 1 cm, the width of PVC sheets was increased to 2.2 cm. Eight 3D printed cubic anchor points with the dimension of 5 mm were glued on edges of the top PVC sheet. The anchor points were placed with a separation distance of 1.75 mm along the width of the PVC sheet, with a separation distance of 7.5 mm along the length of the PVC sheet, and 0.5 cm away from the edges. The schematic views of the disassembled parts of the actuator and the assembled device are shown in Figure 2a,b, respectively. The schematic of the actuator placed on a urinary bladder in a human is illustrated in Figure 2c. The actuator consists of a NiTi spring and a thin SMA wire for the compression phase and two thick SMA wires to define the restoration phase.

Compression Phase. The NiTi spring with 13 total coils and the same dimensions in Figure 1a was prestretched up to 2 cm and then anchored through the holes of two middle anchor points (Figure 2a). A thin SMA wire with the dimensions as in Figure 1a was passed through the spring in Figure 2a. A voltage of 4 V was applied to the SMA wire to heat the spring for the consequent contraction. The reduction of spring's length forced the PVC sheets to bend from upward to downward, thus compressing the balloon or bladder that was placed between the PVC sheets.

Restoration Phase. In order to restore the spring to its extended length, two thick SMA wires with the diameter of 381 μm were passed through 3 anchor points along the length of the PVC sheet (Figure 2a). Only the center anchor points were used to fix the thick SMA wires with glue inside the hole of the anchor point, while both ends of thick SMA wires could move freely inside the hole of the anchor points. After finishing the compression phase, the thick wires were bent along with the PVC sheets. Thus, a 4 V voltage was applied to the thick SMA wires to straighten them. As a result of the straightening of the thick SMA wires, the top bent PVC sheet also was forced to straighten and thus separate from the bottom PVC sheet. This design resulted in the extension of the contracted spring.

The cross sections of the actuator along AA′ and BB′ dotted lines presented in Figure 2a are illustrated in Figure 2d,e. In order to find out the effect of the restoration phase on the operation of the actuator after multiple actuations, first Figure 2d shows the condition of the device at each step by only activating the compression phase. After that, Figure 2e presents the condition of the device at each step by activating both the compression and the restoration phases. In Figure 2d: (i) the actuator was placed on the balloon or bladder, the balloon or bladder was then filled with liquid, and some of the liquid overflowed from the balloon or bladder due to the spring reaction force; (ii) a 4 V voltage was applied to the thin SMA

DOI: 10.1021/acsnano.8b00303
ACS Nano 2018, 12, 3487−3501

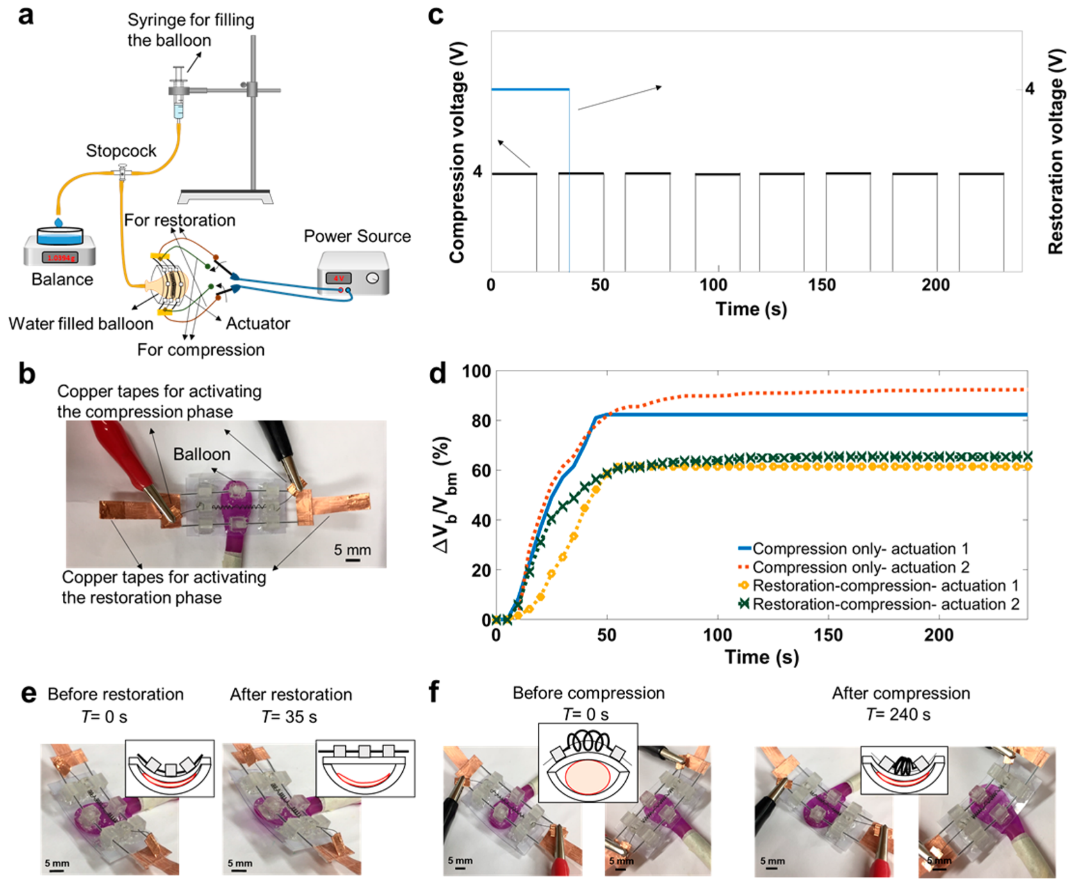

Figure 4. Benchtop experiments for the NiTi spring actuator. (a) The schematic view of the benchtop setup for testing the actuator on a rubber balloon. (b) The image of the actuator on a rubber balloon. (c) The plots of the compression and restoration voltages *versus* time. (d) The curve of voiding percentage *versus* time after two times of compression experiments and two times of restoration−compression experiments for a single spring actuator. (e) The condition of actuator/balloon before and after the restoration phase (the inset schematic views also show the condition). (f) The condition of actuator/balloon before and after the compression phase from two viewing angles (the inset schematic views also show the condition).

wire to heat up the wire thus contracting the spring; (iii) some part of the liquid voided from balloon or bladder due to the spring contraction; (iv) the balloon or bladder was filled again; (v) the filling resulted in an overflow of liquid due to the spring reaction force; and (vi) the thin SMA wire was activated again for the next contraction of the spring and the compression phase. After each cycle of the compression phase, the length of the spring is reduced, and thus the contraction force for the next actuation becomes smaller. In Figure 2e: (i) the actuator was placed on the balloon or bladder, the balloon or bladder was then filled with liquid, and some of the liquid overflowed from balloon or bladder due to the spring reaction force; (ii) a 4 V voltage was applied to the thin SMA wire to heat up the wire and thus contract the spring; (iii) some part of the liquid voided from balloon or bladder due to the spring contraction; (iv) a 4 V voltage was applied to thick SMA wires, thus thick SMA wires restored the spring; and (v) the balloon or bladder was filled with the liquid for the next compression phase. Activating the restoration phase helped to extend the length of spring before each contraction of the spring, and thus more compression force was achieved.

The actuator was modeled using COMSOL to find the optimum thickness of the PVC sheets. The modeled actuator is presented in Figure 3a. A 1 N force, F_b, was applied to the top and bottom PVC sheets to model the force exerted by the filled balloon or bladder to the actuator. Considering the dimensions and stiffness of the spring, a variable force of 0−3 N was applied to the anchor point 1 on the left, F_{sl}, and to the anchor point 2 on the right, F_{sr}, (Figure 3a) to model the forces imposed by the spring. The spring stiffness of the NiTi spring, k_{spring}, is calculated by[52]

$$k_{spring} = \frac{E_{NiTi} d_s^{\,4}}{8 n_s (D_s - d_s)^3} \tag{1}$$

where E_{NiTi} = 83 GPa is the Young's modulus of austenite NiTi.[53]

The schematic of the cross section of the device along the AA′ dotted line (Figure 3a) and the applied forces are shown in Figure 3b. The displacement of the actuator at various thicknesses of the PVC sheets (*i.e.*, 180, 250, and 400 μm) at F_b= 1 N and F_{sr} = F_{sl} = 3 N are presented in Figure 3c−e. The plots of out-of-plane displacement of the top PVC sheet along the Y-axis at F_b = 1 N and various F_{sr} = F_{sl} are illustrated in Figure 3f−h. By increasing the thickness of PVC sheets, the displacement under the same force values reduces. This is due to the increase of spring stiffness of the doubly clamped PVC sheets. The spring stiffness of a doubly clamped PVC sheet, k_{PVC}, is calculated by[54]

$$k_{PVC} = \frac{16 E_{PVC} w h^3}{l^3} \tag{2}$$

DOI: 10.1021/acsnano.8b00303
ACS Nano 2018, 12, 3487−3501

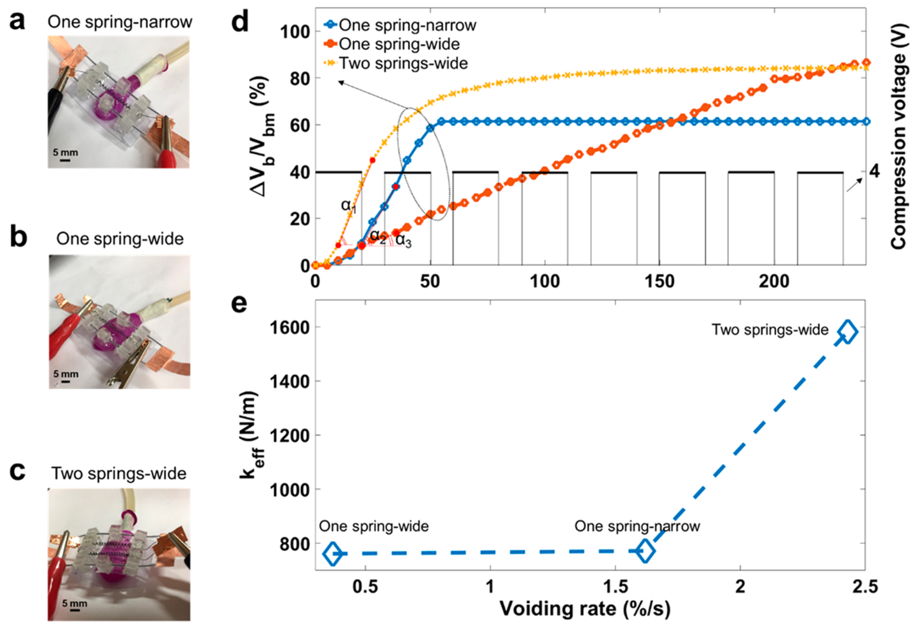

Figure 5. Benchtop experiments for the three actuators with various specifications. The images of actuators tested on a rubber balloon: (a) the one spring-narrow (w = 2.2 cm), (b) the one-spring-wide (w = 2.7 cm), and (c) two spring-wide (w = 2.2 cm) actuators. (d) The curves of voiding percentage and applied compression voltages *versus* time for one spring-narrow, one spring-wide, and two springs-wide actuators. (e) The plot of effective spring stiffness *versus* the voiding rate for the three tested actuators in (a−c).

where E_{PVC} = 1500 MPa is the Young's modulus of PVC,[55] and the effective spring stiffness, k_{eff}, can be calculated as $k_{spring} - k_{PVC}$.

The Benchtop Experiment for the Actuator. The schematic of the benchtop setup used for testing the actuator in Figure 2b on a rubber balloon model of a bladder is shown in Figure 4a. First the actuator was put on a balloon, then the balloon was filled with deionized (DI) water up to 1 mL. The voided water from the balloon, due to the reaction force exerted by the spring, was measured by using a balance to find out the maximum volume of water inside the balloon, V_{bm}. A power source was used to apply 4 V voltage to the thin SMA wire for activating the compression phase and 4 V voltage to thick SMA wires for initiating the restoration phase. The balance was also used for measuring the displaced volume of liquid from the balloon, ΔV_b, after the actuation. The image of the actuator on a rubber balloon is presented in Figure 4b. The 4 V voltage was applied as a series of 8 pulses with the ON state duration of 20 s and OFF state duration of 10 s as shown in Figure 4c. As presented in Figure S1b, 20 s is the suitable time duration to ensure the spring compression upon voltage application. We observed that 10 s time duration was enough for the SMA wire and spring to cool down to some extent before applying the next pulse. For the restoration phase, 4 V was applied for the duration of 35 s to the thick SMA wires since the thick SMA wires require a longer time duration to heat up compared to the thin SMA wire. The curves for restoration and compression voltages *versus* time are presented in Figure 4c. The actuator was actuated four times. The plots of voiding percentage, $\Delta V_b/V_{bm}$, *versus* time for the four actuations are presented in Figure 4d. For the first and the second actuation times, no voltage was applied to the thick SMA wires prior to the compression phase. $\Delta V_b/V_{bm}$ increased rapidly during the first two pulses to 80% for the first actuation and stayed constant afterward. The measured V_{bm} for the first actuation was 0.99 mL. Since V_{bm} reduced to 0.9 mL for the second actuation, $\Delta V_b/V_{bm}$ increased to 90% after two pulses of voltage application. In order to keep V_{bm} constant for each actuation, we first activated the restoration phase followed by the compression phase for the third and fourth actuations. Therefore, V_{bm} for the third and fourth actuations was measured at 0.86 mL. $\Delta V_b/V_{bm}$ for the third and fourth actuations was about 60% after two pulses of voltage application. The reason for lower $\Delta V_b/V_{bm}$ for these actuations can be explained due to the shorter length of the spring after the restoration phase compared to the length of the spring in the first and second actuations due to the forces imposed on the spring by filling of the balloon. The conditions of the actuator and balloon before and after 35 s of applying voltage for the restoration phase are shown in Figure 4e. The application of voltage to thick SMA wires flattened the PVC sheets thus elongated the spring. Figure 4f presents the condition of the actuator and balloon before and after 8 pulses of thin SMA wire activation. The inset schematic views in Figure 4e,f illustrate the condition of the actuator at each step. Note that our technique in this paper achieves a remarkable 60−90% voiding, far exceeding the prior results of 10−20% range.[32,33]

Three actuators were compared together to investigate the effect of PVC width and number of springs on the voiding percentage. First, the number of springs was kept at 1, while w increased from 2.2 cm (Figure 5a) to 2.7 cm (Figure 5b). Then w was kept constant, while the number of springs increased from 1 (Figure 5b) to 2 (Figure 5c). With respect to eq 1, k_{PVC} increased by increasing w. Similarly, by increasing the spring numbers, k_{spring} increased since the total spring stiffness was calculated by summations of the spring stiffness values. Figure 5d shows the plots of $\Delta V_b/V_{bm}$ *versus* time for three actuators after 8 pulses of 4 V voltage application. The compression voltage *versus* time is also presented in Figure 5d. Figure 5e illustrates k_{eff} *versus* maximum slope of the voiding percentage curves, voiding rate, in Figure 5d. The labeled angles of α_1, α_2,

DOI: 10.1021/acsnano.8b00303
ACS Nano 2018, 12, 3487−3501

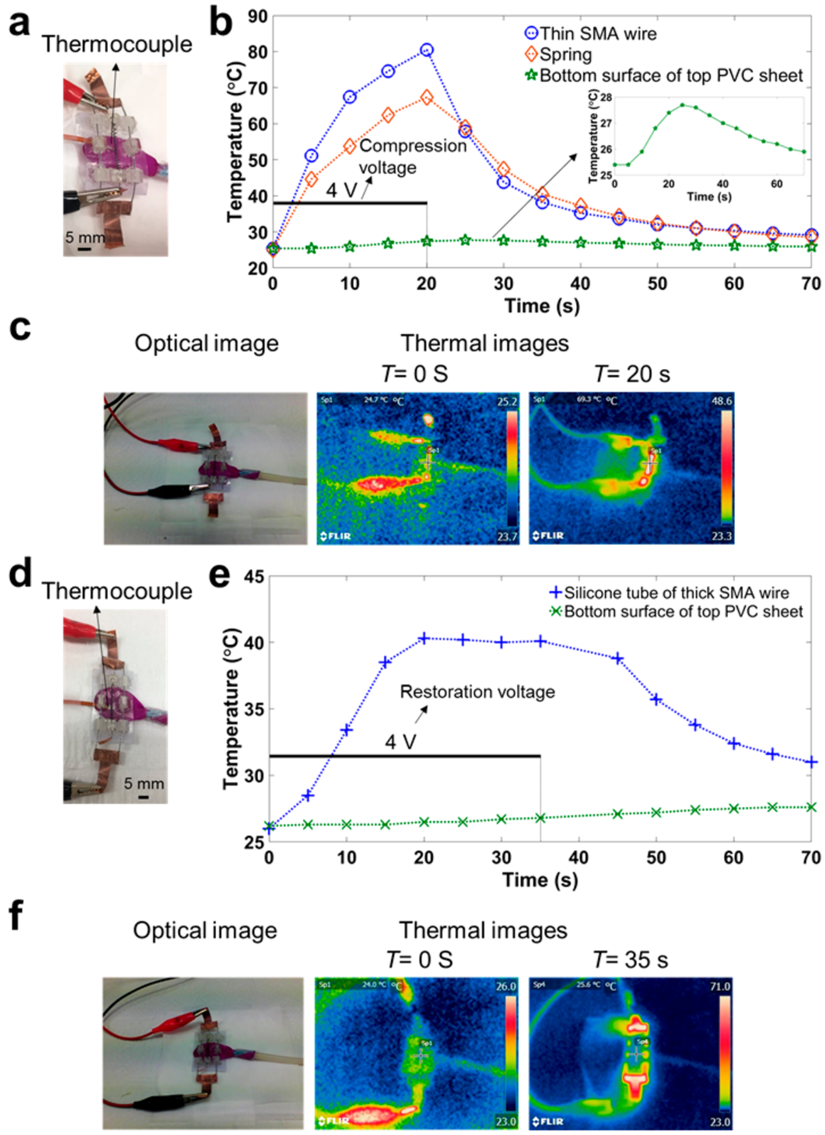

Figure 6. Thermal characterization of the actuator during the compression and restoration phases. The compression phase: (a) The position of the thermocouple under the top PVC sheet underneath the spring. (b) The plot of temperature on the thin SMA wire, the spring, and bottom surface of the top PVC sheet *versus* time. (c) The optical image, and thermal images of the actuator at $T = 0$ s and $T = 20$ s. The restoration phase: (d) The position of the thermocouple under the top PVC sheet underneath the spring. (e) The plot of temperature on the silicone tube of the thick SMA wire and bottom surface of the top PVC sheet *versus* time. (f) The optical image and thermal images of the actuator at $T = 0$ s and $T = 35$ s.

and α_3 in Figure 5d show the points on $\Delta V_b/V_{bm}$ curves that the maximum slope was calculated during 15 s. Higher values for k_{eff} represent higher voiding rates. Based on Figure 5e, higher number of springs and wider PVC sheets can improve the voiding rate from 0.37%/s for the one spring-narrow (w = 2.2 cm) actuator to 2.43%/s for the two springs-wide (w = 2.7 cm) actuator. This result demonstrates the potential of the proposed actuator for application to larger bladder sizes without losing the voiding efficiency. Similarly, thinner PVC thickness should result in a smaller k_{PVC}, thus larger k_{eff} and voiding rate. This is consistent with the simulation results in Figure 3f–h that showed larger displacement changes for thinner PVC sheets. Two PVC sheets with thickness of 400 μm, length of 4 cm, and width of 2.7 cm were used to fabricate an actuator with three integrated springs, as shown in Figure S2a. The plots of $\Delta V_b/V_{bm}$ and compression voltage *versus* time are presented in Figure S2b for three times of actuation. Since the actuator only included the springs for the compression phase, the measured V_{bm} reduced from 2.68 mL for the first actuation, to 1.88 mL for the second actuation, and to 1.41 mL for the last actuation, and $\Delta V_b/V_{bm}$ varied similarly to the first two actuations in Figure 4d. A voiding rate of 0.57%/s was calculated for the second actuation with respect to the labeled angle, α_4, in Figure S2b. This level of voiding rate shows the importance of the PVC thickness on the amount of water voided from the balloon after the compression. The condition of the actuator seen from two angles on a filled balloon before the actuation is presented in Figure S2c. Figure S2d shows the condition of the actuator from two view angles and the voided balloon after the completion of the compression phase at T = 330 s.

The temperature change of the thin SMA wire and spring during the compression phase of the actuator for one pulse of 4 V voltage application was measured by using a FLUKE 52 II

DOI: 10.1021/acsnano.8b00303
ACS Nano 2018, 12, 3487–3501

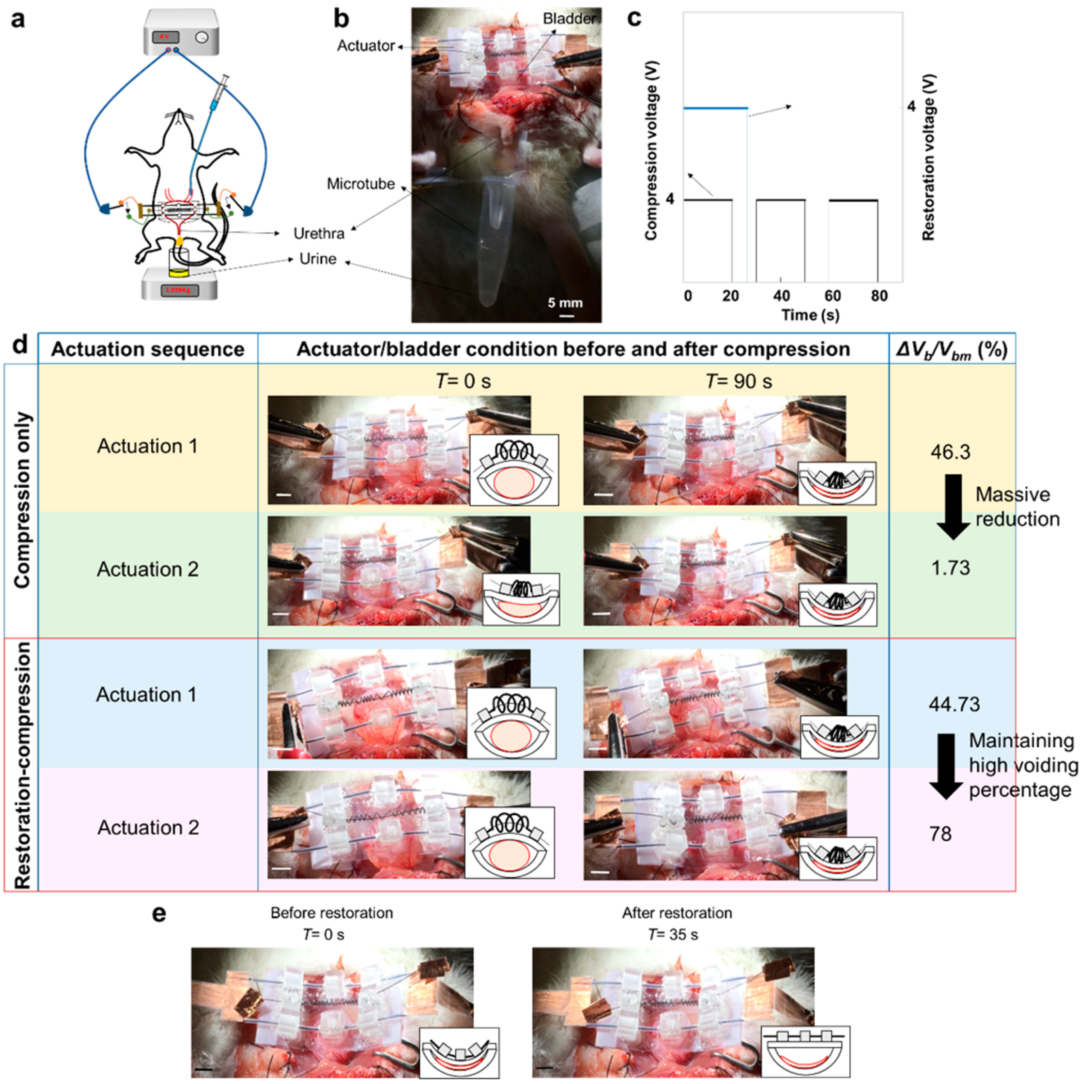

Figure 7. *In vivo* **test of the spring actuator in an anesthetized rat. (a) The schematic of the** *in vivo* **setup for testing of the actuator in a rat model. (b) The applied device on the bladder. (c) The applied compression and restoration voltages to the actuator for the** *in vivo* **test. (d) The condition and voiding percentage of the one spring-narrow actuator during four consecutive actuations before and after the compression phases completed and the inset schematic views for each condition (the scale bar is 5 mm). (e) The device before and after the restoration phase and the inset schematic views for each condition (the scale bar is 5 mm).**

thermometer (Everett, WA). A K-type thermocouple was positioned first on the surface of the thin SMA wire and then on the surface of the spring. After that, we positioned the thermocouple under the bottom surface of the top PVC sheet under the spring (Figure 6a) to measure the amount of temperature increase on the balloon or bladder surface. The curves of temperature on the thin SMA wire, spring, and bottom surface of the top PVC sheet *versus* time are presented in Figure 6b. The temperature of the thin SMA wire reached from 25.4 °C at $T = 0$ s to 80.5 °C at $T = 20$ s, while the temperature of spring reached from 25.4 °C at $T = 0$ s to 67.3 °C at $T = 20$ s. A maximum temperature increase of 2 °C was observed for the bottom surface of the top PVC sheet after heating of the thin SMA wire for 20 s as shown as inset to Figure 6b. The current actuating design shows a very much lower and, thus, safer operation temperature compared to the previous interlaced SMA actuator which had a temperature increase of about 17 °C on the surface of the balloon underneath the SMA wires.[33] Since the actuator is activated infrequently for bladder control, the small heat is dissipated, and as such this small temperature change would be tolerated. A FLIR E5 thermal imaging camera (Wilsonville, OR) was also used to monitor the temperature change of the whole spring device upon voltage application. The optical image and thermal images of the device at $T = 0$ s and $T = 20$ s are shown in Figure 6c.

The temperature measurement for the actuator was also carried out during the restoration phase. The temperature on the surface of the silicone tube of thick SMA wires and the bottom surface of top PVC sheet under the spring was measured with the thermocouple (Figure 6d). The temperature profiles of the silicone tube surface and the surface bottom of the PVC sheet are shown in Figure 6e. The temperature of the silicone tube increased from 26.2 °C at $T = 0$ s to 40.1 °C at $T = 35$ s. The temperature of the bottom surface of top PVC sheet under the spring showed an increase of about 0.7 °C after applying a 4 V voltage to thick SMA wires for 35 s. The temperature increase at the bottom surface of top PVC sheet under each SMA thick wire was about 1 and 1.3 °C. The optical

DOI: 10.1021/acsnano.8b00303
ACS Nano 2018, 12, 3487−3501

image and thermal images of the device during the restoration phase at T = 0 s and T = 35 s are also presented in Figure 6f.

***In Vivo* Animal Test of the Actuator.** The *in vivo* experiment setup for testing the actuator on a rat's bladder is illustrated in Figure 7a. The actuator was first placed on the bladder, and then the bladder was filled with saline volume of up to 1 mL through a microcannula that was inserted in the ureter. The excess urine overflowing from the bladder was weighed using a balance. A density of 1.0012 kg/L was measured for the voided liquid from bladder.[32] Figure 7b presents the actuator that is placed on a bladder. Our *in vivo* experiment was carried out in two steps to clarify the importance of adding a restoration phase for the actuator. The first step only includes the compression phase, while for the second step, the restoration phase was also added to the compression phase.

Compression Only Phase. Two actuations were done by applying 4 V voltage as consecutive three pulses of 20 s for activating the compression only phase as presented in Figure 7c. Since the one spring-narrow actuator in Figure 5d reached the maximum voiding percentage during the third voltage pulse, we reduced the number of pulses from 8 in the balloon experiment to 3 pulses for the *in vivo* test. After the first actuation, the spring contracted, and this resulted in 46.3% of voiding for the measured V_{bm} of 1 mL. For the next actuation, since the bladder Young's modulus[56] is much smaller than that of the rubber balloon,[57] the spring could not be elongated due to the filling of the bladder. Therefore, the bladder expanded horizontally between the collapsed PVC sheets in contrast to the balloon that could separate the PVC sheets during the filling process. Thus, V_{bm} was measured at the same value of 1 mL. Since the spring was at its compressed condition, the second compression phase led to a small voiding percentage of 1.73%. The conditions of the actuator/bladder before (T = 0 s) and after the completion of compression phase (T = 90 s) are shown in Figure 7d.

Restoration–Compression Phase. In order to overcome the huge reduction in the voiding percentage for the second actuation in the step 1, a restoration phase is initiated prior to the compression phase for each actuation in the step 2. The restoration voltage *versus* time plot is shown in Figure 7c. We first activated the restoration phase to restore the spring to a longer length for achieving high levels of voiding percentage after each time of actuation. By activating the restoration phase prior to the compression phase, the high voiding percentages of 44.73% and 78% were maintained for the first and second actuations, respectively. The conditions of the actuator/bladder before (T = 0 s) and after the completion of the compression phase (T = 90 s) are shown in Figure 7d. The conditions of the actuator before (T = 0 s) and after the restoration phase (T = 35 s) are presented in Figure 7e. The schematic views for each condition are presented as insets to Figure 7d,e. The maximum volume of liquid in the bladder or balloon and the liquid volume voided for the actuations in Figures 4 and 7 are summarized in Table S1. Movie S2 shows the restoration phase of the actuator, while the compression phase and voiding of the bladder is presented in Movie S3. As seen in Movie S2, the voiding of the bladder completed about 17 s after the voltage was turned ON. Also, the straightening of the bent thick SMA wires completed after 15 s after applying the voltage (Movie S3).

There might be a concern about backflow of urine toward kidneys especially after the completion of the compression phase. This is due to the fact that since the filling rate of urine in the urinary system is slow,[58] the forces imposed by bladder during the filling may not be large enough to open the PVC sheets. Activating the restoration phase after the completion of each compression phase and prior to the next step of compression not only helped to elongate the spring but also opened the PVC sheets to ease filling of bladder and avoid backflow of urine. Movie S4 presents the filling of the bladder with saline with a filling rate of 3 μL/s after activating the restoration phase. It should be obvious that the force due to the bladder filling overcame the compressed spring.

The characteristics of the spring actuator in this work (*i.e.*, voiding percentage, number of activations per 327 s, and total energy consumption) were compared to the previously proposed SMA-based actuators. The images of the three actuators on a rubber balloon are shown in Figure 8a. The curves of voiding percentage *versus* time for the actuators are presented in Figure 8b. The spring actuator showed an increase of about 5 times and 12 times in the voiding percentage after 20 s of voltage application compared to the interlaced and parallel

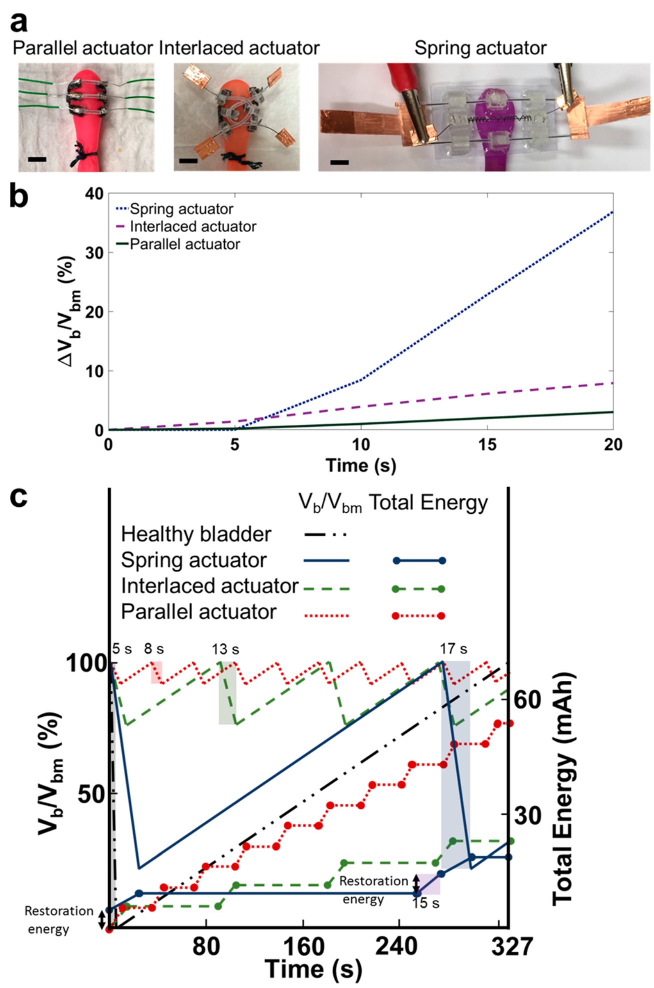

Figure 8. A comparison of the previously proposed actuators and the spring actuator in this work. (a) The images of the parallel, interlaced, and spring actuators (the scale bar is 5 mm). (b) The curve of voiding percentage *versus* time for the three actuators under 4 V voltage application for 20 s. (c) The plots of percentage of the liquid volume in the bladder, V_b/V_{bm}, *versus* time and the total energy consumption during 327 s for the three actuators in (a).

DOI: 10.1021/acsnano.8b00303
ACS Nano 2018, 12, 3487–3501

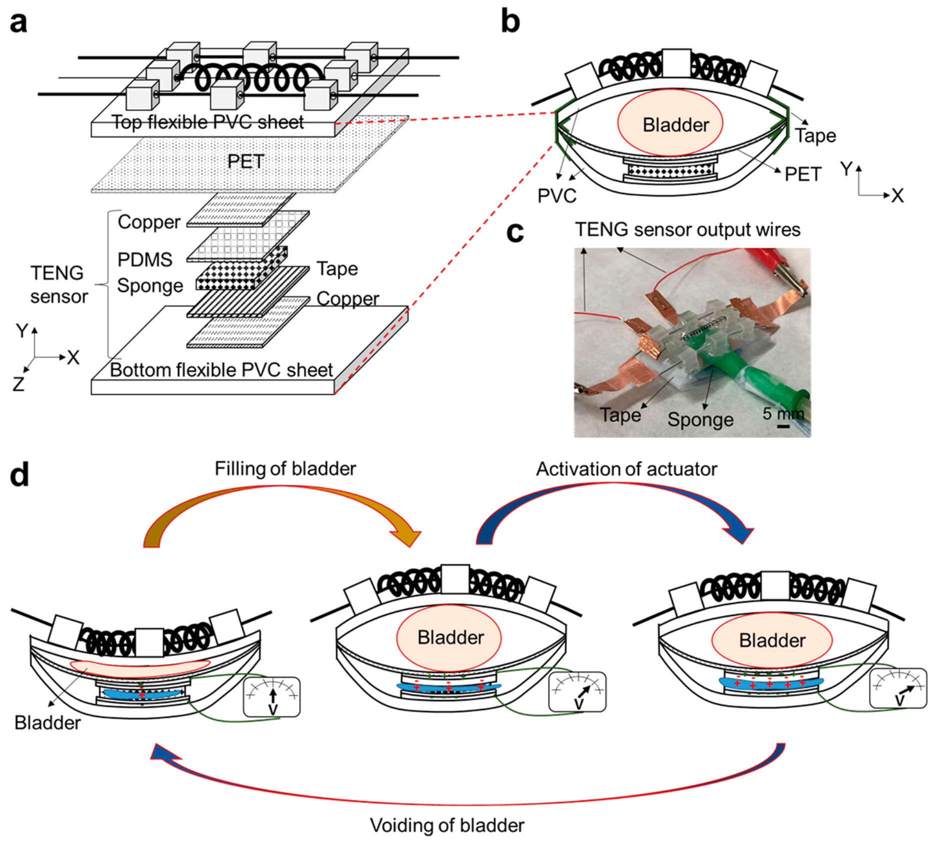

Figure 9. Integration of the TENG sensor with the spring actuator. (a) The schematic view of the disassembled device. (b) The schematic view of the assembled device. (c) The image of the device on a rubber balloon. (d) The schematic view of the operation of the integrated device during the filling of the balloon or bladder and the activation of the actuator.

devices, respectively. We compared the number of activations required for voiding the bladder during 327 s for the three actuators in comparison with a healthy rat's bladder in Figure 8c. Considering a 5 s time period for a rat to completely void the bladder, a time period of 8, 13, and 17 s was observed for the parallel, interlaced, and spring actuators, respectively, to void the bladder up to the maximum possible voiding percentage. The percentage of the liquid volume in the bladder, V_b/V_{bm} *versus* time for the activations is presented in Figure 8c. While a healthy bladder of a rat voids one time per 327 s, the maximum voiding percentage of 8.12% for the parallel device resulted in 10 times of activations during this time period. The number of activations reduced to 4 times for the interlaced device with the maximum voiding percentage of 23.59%. The spring actuator with the highest voiding percentage of 78% led to only 2 times of activations per 327 s. The total energy consumption for the three actuators *versus* time is also shown in Figure 8c. The total energy consumption including the energy for the restoration phase of the spring actuator was about 19.59 mAh and lower than that of 23.04 mAh and 54.56 mAh for the parallel and interlaced actuators, respectively.

Since the voiding of the bladder completed only after 17 s of voltage application during the compression phase, and based on the thermal characterization in Figure 6b, a maximum temperature increase of 1.5 °C would be expected at $T = 17$ s for the bladder surface. Similarly, due to the completion of the restoration phase after 15 s of voltage application to thick SMA wires, the temperature increase would be about 0.1 °C on the bladder surface. This level of temperature increase is within the acceptable temperature increase for an implantable device.[59]

The Triboelectric Nanogenerator Sensor Design and Sensing Mechanism. The operation of TENGs is based on alternate contact and separation of two surfaces with different electron affinities.[60,61] In this scenario, after each contact–separation cycle, one transit spike output would be generated.[62,63] By placing a TENG sensor between the balloon or bladder surface and the bottom PVC sheet, we are able to monitor the changes in the volume of the balloon or bladder during filling with liquid. However, the two surfaces of the TENG sensor were always in the contact mode during filling, therefore, the common spike output of the TENG as a nanogenerator is not expected for the sensing application in this work. For this reason, we designed a wet sponge-based TENG sensor that was proposed recently.[64] The schematic of the disassembled layers of the sensor is presented in Figure 9a. A thin polyethylene terephthalate (PET) layer was placed between the PVC sheets. Copper electrodes were attached to the bottom surface of the PET layer and top surface of the bottom PVC sheet. A polydimethylsiloxane (PDMS) layer and a 1 mm-thick sponge layer containing 0.2 mL of DI water were sandwiched between copper electrodes. The assembled layers of the TENG sensor in Figure 9a were assembled as illustrated in Figure 9b, and the balloon or bladder was placed between the top PVC sheet and the PET layer. The assembled actuator and sensor on a rubber balloon are presented in Figure 9c.

The sensing mechanism for the sensor is shown in Figure 9d. When the bladder or balloon was empty, the water stayed inside the sponge, and therefore, the output voltage due to the

DOI: 10.1021/acsnano.8b00303
ACS Nano 2018, 12, 3487−3501

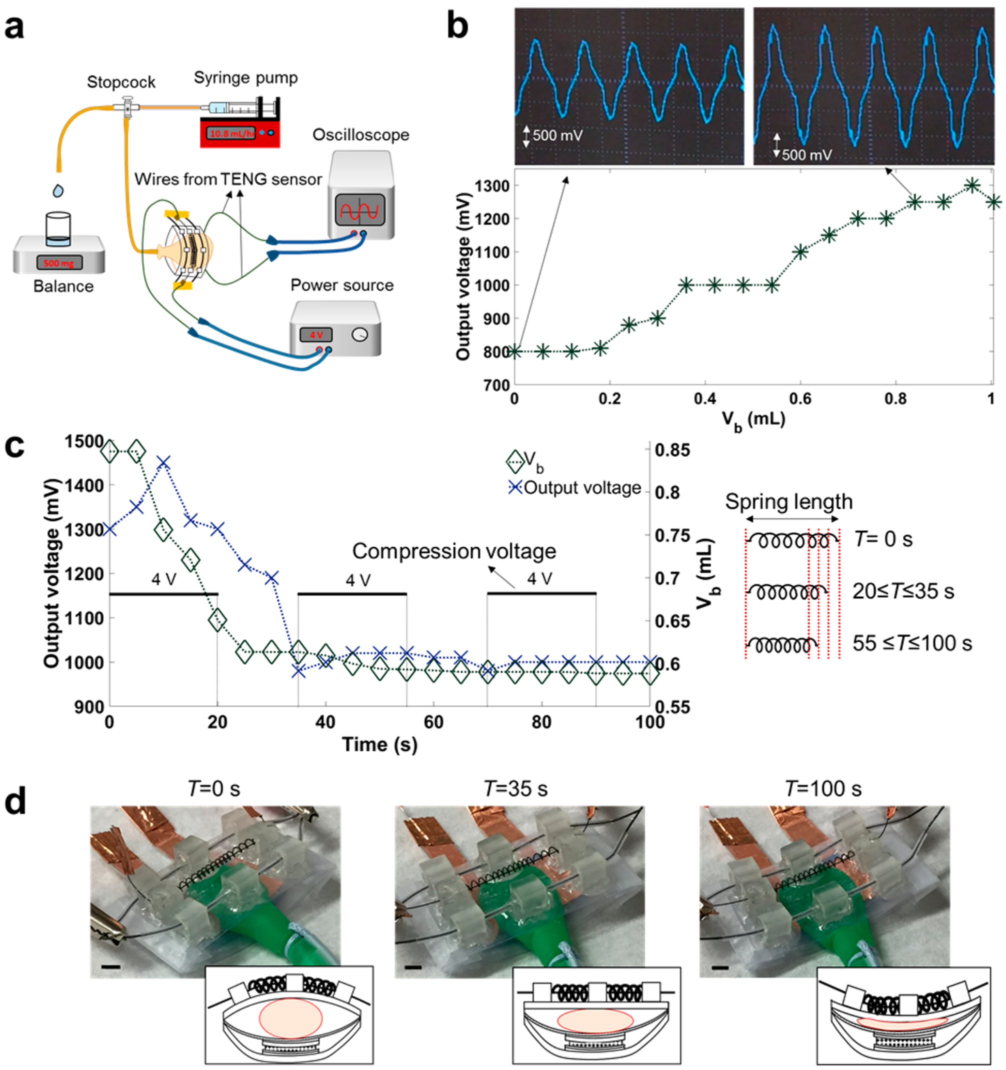

Figure 10. Benchtop experiment for the integrated device. (a) The schematic view of the benchtop setup. (b) The plot of the TENG output voltage *versus* V_b during the filling of the balloon. The output voltage plots at V_b = 0 and 0.84 mL are also shown as insets to (b). (c) The curve of the TENG output voltage and V_b *versus* time during the activation of the actuator by applying a 4 V compression voltage (the change of the spring length during the compression is also shown). (d) The condition of the device in (c) at T = 0, 35, and 100 s and inset schematic views for each condition.

triboelectrification and electrostatic induction between the PDMS layer, water, and copper electrodes was at its minimum level. By filling the balloon or bladder with liquid, the water gradually squeezed out of the sponge and became exposed to the PDMS layer, and thus the output voltage increased. When the balloon or bladder was almost full and the output voltage became constant, the actuator was activated, thus a sudden force imposed onto the TENG sensor and squeezed more water out of the sponge. As a result, a sudden increase in the output voltage was observed. The balloon or bladder started to void due to the activation of the actuator, thus the water started to go back inside the sponge, and consequently, the output voltage reduced.

Prior to the integration of the TENG sensor with the actuator, we used a range of weights from 20 g up to 700 g to measure the output voltage of the sponge-based TENG sensor for a range of applied forces. The sponge contained 0.2 mL of DI water. The curve of the output voltage *versus* force is presented in Figure S3a, and the schematic side view of the sensor is shown in Figure S3b. The output voltage of the sensor in Figure S3a increased from 35.6 mV to 114 mV by increasing the applied force from 0 to 6.86 N. The schematic side view of the sensor after adding a weight on top of the sensor is illustrated in Figure S3c. The output voltage of the sensor *versus* time for various applied weights from 20 to 700 g are presented in Figure S3d. The parts of the output voltage curves that are labeled with the dotted lines in Figure S3d present the output voltage increase at the time that the weight was placed on top of the sensor. The output voltage of the TENG sensor was a sinusoidal-like signal in which the peak level of the signal changed after adding the weights on top of the sensor.

The Benchtop Experiment for the TENG Sensor Integrated with the Actuator. The schematic of the benchtop setup used for testing the integrated TENG sensor with the actuator is shown in Figure 10a. First, the device was placed on a rubber balloon, and the output wires from the sensor were connected to an oscilloscope. Then, A 4 V voltage was applied to thick SMA wires for the restoration phase, and a syringe pump was used to fill the balloon with a constant flow rate of 3 μL/s up to 1 mL. Similar to the output voltage in

DOI: 10.1021/acsnano.8b00303
ACS Nano 2018, 12, 3487−3501

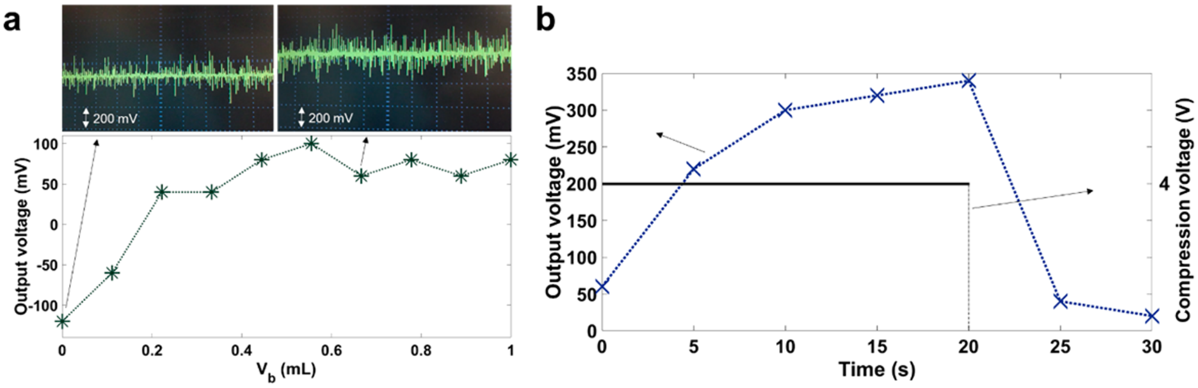

Figure 11. *In vivo* **test of the integrated device in an anesthetized rat. (a) The curve of the TENG output voltage** ***versus*** V_b **during the filling of the bladder. The output voltage plots at** V_b= **0 and 0.67 mL are shown as insets to (a). (b) The plots of the TENG output voltage and compression voltage** ***versus*** **time during the activation of the actuator.**

Figure S3d, the output voltage of the integrated TENG sensor was a sinusoidal-like signal, and peak level of the signal increased during the experiment. Therefore, the peak of the signal was considered as an indicator for studying the effect of filling and voiding of the balloon on the sensor. The integration of the TENG sensor with the actuator caused an increase in the initial output voltage as shown in Figure 10b. The maximum output voltage in Figure 9b started to increase by filling the balloon with water. The curve of the output voltage *versus* the liquid volume in the balloon, V_b, is shown in Figure 10b. The output voltage plots at V_b= 0 and 0.84 mL are presented as insets to Figure 10b. Movie S5 shows the changes of the output voltage of the sensor during the filling of the balloon. The stopcock was left open so the excess water from the balloon voided from the balloon; V_b reduced from 1 to 0.84 mL which was the same V_b value in Figure 10b at which the output voltage started to saturate. Therefore, this value for V_b may be used as a sign for a full bladder with the maximum volume of V_{bm} and the correct time for activating the actuator.

The 4 V compression voltage was applied in a pulsed manner with the ON state duration of 20 s and OFF state duration of 15 s as shown in Figure 10c. The spring started to contract, and the voided water from the balloon was measured by using a balance. At the same time, the output voltage of the TENG sensor was monitored by the oscilloscope. The plots of output voltage and V_b *versus* time are also presented in Figure 10c. A schematic on the reduction of the spring length during each pulse of compression voltage application is illustrated in Figure 10c. For the first pulse of the compression voltage, during the first 10 s, a sudden force was imposed from the contracted spring to the sensor, thus a sudden increase in output voltage was observed. However, the output voltage started to decrease afterward since the water voided from the balloon and less force was exerted from the balloon onto the sensor. A similar response to the output voltage curve for the first pulse was observed for the second pulse. Since V_b already reduced during the second pulse, the changes of output voltage were smaller than that of the first pulse. Changes of output voltage during the third pulse was almost constant since the voiding of water completed. A $\Delta V_b/V_{bm}$ of about 30% was calculated for the device that was less than the voiding percentage of about 60% achieved for the actuator only in Figure 4d. This was due to the fact that adding of the TENG sensor to the actuator increases the total spring stiffness of PVC sheets, thus the voiding percentage reduced. The images of the device during the activation in Figure 10c at T = 0, 35, and 100 s are shown in Figure 10d. The inset schematic views also represents the condition of the actuator at each time.

In Vivo **Animal Test of the TENG Sensor Integrated with the Actuator.** The *in vivo* experiment setup in Figure 7a was used to measure the TENG sensor integrated with the actuator. The device was put on an empty bladder, and a 4 V voltage was applied to the thick SMA wires for the restoration phase. The output wires of the TENG sensor were connected to the oscilloscope. The bladder was then filled with saline volume of up to 1 mL, and the changes in the output voltage were monitored. The curve of output voltage *versus* V_b is presented in Figure 11a. Contrary to the sinusoidal-like output voltage of the device in the benchtop experiment setup, the output voltage of the sensor in the animal test was a DC signal due to the effect of bladder surface charge and presence of body fluid. The level of DC signal changed during the filling and voiding of the bladder. The output voltage increased by increasing V_b similar to Figure 10b. The voltage started to saturate at about V_b= 0.67 mL. Movie S6 presents the changes of the output voltage during the filling of the bladder.

A 4 V voltage was applied to the actuator for the duration of 20 s. The output voltage *versus* time is presented in Figure 11b. Similar to Figure 10c, the voltage increased due to the contraction force imposed by the spring onto the sensor. The increase of voltage in Figure 11b (in contrast to Figure 10c) continued during the 20 s of voltage application. This was due to the fact that while the bladder was less stiff than the rubber balloon, the voiding of the bladder completed during 20 s of voltage application. Therefore, the force imposed onto the sensor continued until the removal of voltage. After removing the activation voltage, the output voltage of the sensor started to decrease and reached a value smaller than the starting output voltage value since the bladder was emptied by the actuator. Considering V_{bm} of 0.79 mL, a voiding percentage of 43.8% was calculated for the device; this percentage was smaller than that for the animal test results for the actuator only in Figure 7d. This difference between the voiding percentage of the integrated device and the actuator only was also observed for Figure 10c. The actuation of the device and changes of the output voltage during the actuation are shown in Movies S7 and S8, respectively. Movies S7 and S8 were shot at the same time.

The actuator reported here exploits a mechanism and operation to physically contract the detrusor muscle. The

DOI: 10.1021/acsnano.8b00303
ACS Nano 2018, 12, 3487−3501

achieved voiding percentage of approximately 60% of the bladder upon a few seconds of actuation shows the potential for this actuator to replace the common ureteric catheters used in patients with detrusor underactivity. The device was successfully implanted in an anesthetized rat, however, for the future implantation of the device in an awake rat, the NiTi spring should be encapsulated to avoid any interaction with other tissues to allow its free movement during the actuation. The encapsulation material should be soft enough not to interrupt the normal compression and restoration of the spring.

The integration of this actuator with a flexible TENG sensor for detecting the fullness of the bladder can enable us to build an autonomous system for full control of the bladder voiding for neurogenic UAB patients with both damaged detrusor muscle and nervous system, especially for patients with insufficient manual dexterity or hesitant body behavior. The TENG sensor not only can detect the bladder fullness, but also its output voltage can be used for charging of a supercapacitor in future that later powers the actuator. Future wireless transfer of the sensor output signal to the patient as a control signal allows the patient to activate the actuator and void the bladder on his/her own.

Replacing of the sponge with a biocompatible hydrogel or encapsulating it with a PDMS frame and usage of biocompatible materials for 3D printing of the anchor points should help make the whole system biocompatible and feasible for future clinical applications.

CONCLUSION

In summary, we present a highly efficient actuator based on microscale diameter NiTi SMA wires and springs. The atomic-level structural changes in the NiTi spring due to the heating of the thin SMA wire resulted in the bistable mechanism of the flexible sheets. The dependence of the actuator characteristics on the dimension of flexible sheets and the number of springs was studied. In the presence of combined compression and restoration phases, a remarkably high voiding percentage after each actuation, significantly exceeding current state of the art, was successfully achieved for the benchtop test and *in vivo* experiment on an anesthetized rat's bladder. Moreover, this capability allows multiple actuations of the device for achieving a complete void in the case of larger bladder sizes or stiffer bladder muscles. Our idea of building in a restoration phase results in a high level of sustained efficiency in voiding. Integration of a TENG sensor for detecting the fullness of bladder for neurogenic UAB patients with degraded nerve function provides a proof-of-concept for making a self-controlled system for future clinical application.

EXPERIMENTAL SECTION

Materials. SMA wires were purchased from Dynalloy Inc. (Irvine, CA). The PDMS layer was purchased from Interstate Inc. (Sutton, MA), and NiTi springs were purchased from Kellogg's Research Laboratories (Hudson, NH). Common PVC binding sheets were used for fabricating the actuator. 50 μm-thick tape was purchased from Deli Group Co. Ltd. (China). Object260 Connex3 printer was used to 3D print anchor points with hole diameters of 2.5 mm with the VeroClear-RGD810 material.[65]

Actuator Fabrication. Two PVC sheets were joined together with the 50 μm-thick tape along their width. Eight anchor points were glued on the surface of top PVC sheet. The NiTi spring was then cut in the desired length and anchored to the anchor points with ultraviolet (UV) curable glue. The thin SMA wire was then passed through the assembled spring. Thick SMA wires were covered with silicone tubing and passed through anchor points. Each thick SMA wire was only fixed by glue to the middle anchor point. Copper tape was applied to the ends of each SMA wire for easier connection of power source to the device.

TENG Sensor Fabrication. A thin 50 μm-thick PET layer with the same dimensions as the PVC sheets was placed between them, and they were joined with the 50 μm-thick tape along their width. The PET layer was used for fixing the TENG sensor. 70 μm-thick copper tape electrodes with the dimensions of 1.4 cm × 2.2 cm ($w \times l$) were attached to center of the bottom surface of the PET layer and top surface of the bottom PVC sheet. The bottom copper electrode was covered with 50 μm-thick tape in order to avoid its contact with the wet sponge. A 431.8 μm-thick polydimethylsiloxane (PDMS) layer with the dimension of 1.4 cm × 2.2 cm ($w \times l$) and a 1 mm-thick sponge layer containing 0.2 mL of DI water and with the dimension of 1.4 cm × 2.2 cm ($w \times l$) were sandwiched between copper electrodes.

Surgical Procedure. The experiments were performed on two adult female Sprague−Dawley rats (300 g). The animal care and use procedures were approved by the Institutional Animal Care and Use Committee (IACUC) of the National University of Singapore. The methods were carried out in accordance with the R15-0592 protocol. The animal was anaesthetized by injecting ketamine-xylazine (75 mg/kg-10 mg/kg) into the intraperitoneal space. Carprofen (5 mg/kg) and normal saline (0.2−0.5 mL/10g) were injected subcutaneously to provide analgesic and prevent dehydration of the animal. After exposing the bladder, the actuator was put on the bladder and filled with normal saline to carry out the experiments.

ASSOCIATED CONTENT

Supporting Information

The Supporting Information is available free of charge on the ACS Publications website at DOI: 10.1021/acsnano.8b00303.

(Figure S1) One spring actuator on a single PVC sheet; (Figure S2) Spring-based actuator with three springs; (Table S1) Liquid volume in the balloon or bladder; (Figure S3) Characterization of the TENG sensor (PDF)

Movie S1: Actuation of the one spring actuator on a single PVC sheet (MOV)

Movie S2: Restoration phase (MOV)

Movie S3: Compression phase (MOV)

Movie S4: Filling of the bladder in the presence of the actuator (MOV)

Movie S5: Filling of the balloon in the presence of the integrated device (MOV)

Movie S6: Filling of the bladder in the presence of the integrated device (MOV)

Movie S7: Voiding of the bladder in the presence of the integrated device (MOV)

Movie S8: Output voltage of the TENG sensor during the voiding of the bladder (MOV)

AUTHOR INFORMATION

Corresponding Authors

*E-mail: faezeh.arabhassani@gmail.com.
*E-mail: shihcheng@nus.edu.sg.
*E-mail: sinapsedirector@gmail.com.
*E-mail: elelc@nus.edu.sg.

ORCID

Faezeh Arab Hassani: 0000-0003-4425-6289
Chengkuo Lee: 0000-0002-8886-3649

Author Contributions

F. A. Hassani, H. Wang, and C. Lee: device design concept. F. A. Hassani: device modeling, fabrication, and characterization. F. A. Hassani and S.-C. Yen: experimental design and setup and

DOI: 10.1021/acsnano.8b00303
ACS Nano 2018, 12, 3487−3501

in vivo test data interpretation. R. O. Mogan and G. G. L. Gammad: animal surgeries. F. A. Hassani: *in vivo* test setup and device implantation on bladder. S.-C. Yen, N. V. Thakor, and C. Lee: principal investigators, study design, data interpretation. All authors have given approval to the final version of the manuscript.

Funding

The authors would like to acknowledge financial support from following research grants: NRF-CRP10-2012-01 'Peripheral Nerve Prostheses: A Paradigm Shift in Restoring Dexterous Limb Function' and NRF-CRP8-2011-01 'Self-powered body sensor for disease management and prevention-orientated healthcare' from the National Research Foundation (NRF), Singapore, Faculty Research Committee (FRC) grant- R-263-000-B56-112 'Thermoelectric power generator (TEG) based self-powered ECG plaster— System integration (Part 3)' at the National University of Singapore, Singapore, and HIFES Seed Funding-2017-01 grant R-263-501-012-133 'Hybrid integration of flexible power source and pressure sensors' at the National University of Singapore, Singapore.

Notes

The authors declare no competing financial interest.

ACKNOWLEDGMENTS

The authors would also like to thank T. K. Ng, T. L. C. Kuo, L. G. Ng, and P. Luu for providing the idea for a bladder contraction device.

REFERENCES

(1) Choi, S.; Lee, H.; Ghaffari, R.; Hyeon, T.; Kim, D.-H. Recent Advances in Flexible and Stretchable Bio-Electronic Devices Integrated with Nanomaterials. *Adv. Mater. (Weinheim, Ger.)* **2016**, *28*, 4203–4218.

(2) Pang, C.; Lee, C.; Suh, K.-Y. Recent Advances in Flexible Sensors for Wearable and Implantable Devices. *J. Appl. Polym. Sci.* **2013**, *130*, 1429–1441.

(3) Wang, C.; Hwang, D.; Yu, Z.; Takei, K.; Park, J.; Chen, T.; Ma, B.; Javey, A. User-Interactive Electronic Skin for Instantaneous Pressure Visualization. *Nat. Mater.* **2013**, *12*, 899–904.

(4) Boutry, C. M.; Nguyen, A.; Lawal, Q. O.; Chortos, A.; Rondeau-Gagné, S.; Bao, Z. A Sensitive and Biodegradable Pressure Sensor Array for Cardiovascular Monitoring. *Adv. Mater. (Weinheim, Ger.)* **2015**, *27*, 6954–6961.

(5) Huang, X.; Liu, Y.; Cheng, H.; Shin, W.-J.; Fan, J. A.; Liu, Z.; Lu, C.-J.; Kong, G.-W.; Chen, K.; Patnaik, D.; Lee, S.-H.; Hage-Ali, S.; Huang, Y.; Rogers, J. A. Materials and Designs for Wireless Epidermal Sensors of Hydration and Strain. *Adv. Funct. Mater.* **2014**, *24*, 3846–3854.

(6) Koo, J. H.; Jeong, S.; Shim, H. J.; Son, D.; Kim, J.; Kim, D. C.; Choi, S.; Hong, J.-I.; Kim, D.-H. Wearable Electrocardiogram Monitor Using Carbon Nanotube Electronics and Color-Tunable Organic Light-Emitting Diodes. *ACS Nano* **2017**, *11*, 10032–10041.

(7) Liu, Y.; Pharr, M.; Salvatore, G. A. Lab-on-Skin: A Review of Flexible and Stretchable Electronics for Wearable Health Monitoring. *ACS Nano* **2017**, *11*, 9614–9635.

(8) Park, S. I.; Brenner, D. S.; Shin, G.; Morgan, C. D.; Copits, B. A.; Chung, H. U.; Pullen, M. Y.; Noh, K. N.; Davidson, S.; Oh, S. J.; Yoon, J.; Jang, K.-I.; Samineni, V. K.; Norman, M.; Grajales-Reyes, J. G.; Vogt, S. K.; Sundaram, S. S.; Wilson, K. M.; Ha, J. S.; Xu, R.; et al. Soft, Stretchable, Fully Implantable Miniaturized Optoelectronic Systems for Wireless Optogenetics. *Nat. Biotechnol.* **2015**, *33*, 1280–1286.

(9) Xu, L.; Gutbrod, S. R.; Bonifas, A. P.; Su, Y.; Sulkin, M. S.; Lu, N.; Chung, H.-J.; Jang, K.-I.; Liu, Z.; Ying, M.; Lu, C.; Webb, R. C.; Kim, J.-S.; Laughner, J. I.; Cheng, H.; Liu, Y.; Ameen, A.; Jeong, J.-W.; Kim, G.-T.; Huang, Y.; Efimov, I. R.; Rogers, J. A. 3D Multifunctional Integumentary Membranes for Spatiotemporal Cardiac Measurements and Stimulation Across the Entire Epicardium. *Nat. Commun.* **2014**, *5*, 3329.

(10) Park, A. H.; Lee, S. H.; Lee, C.; Kim, J.; Lee, H. E.; Paik, S.-B.; Lee, K. J.; Kim, D. Optogenetic Mapping of Functional Connectivity in Freely Moving Mice *via* Insertable Wrapping Electrode Array Beneath the Skull. *ACS Nano* **2016**, *10*, 2791–2802.

(11) Viventi, J.; Kim, D.-H.; Vigeland, L.; Frechette, E. S.; Blanco, J. A.; Kim, Y.-S.; Avrin, A. E.; Tiruvadi, V. R.; Hwang, S.-W.; Vanleer, A. C.; Wulsin, D. F.; Davis, K.; Gelber, C. E.; Palmer, L.; Van der Spiegel, J.; Wu, J.; Xiao, J.; Huang, Y.; Contreras, D.; Rogers, J. A.; Litt, B. Flexible, Foldable, Actively Multiplexed, High-Density Electrode Array for Mapping Brain Activity *In Vivo*. *Nat. Neurosci.* **2011**, *14*, 1599–1605.

(12) Heo, D. N.; Kim, H.-J.; Lee, Y. J.; Heo, M.; Lee, S. J.; Lee, D.; Do, S. H.; Lee, S. H.; Kwon, I. K. Flexible and Highly Biocompatible Nanofiber-Based Electrodes for Neural Surface Interfacing. *ACS Nano* **2017**, *11*, 2961–2971.

(13) Stoeckel, D. Shape Memory Actuators for Automotive Applications. *Mater. Eng.* **1990**, *11*, 302–307.

(14) Huang, W. *Shape Memory Alloys and their Application to Actuators for Deployable Structures*. Ph.D. Thesis, The University of Cambridge, United Kingdom, March 1998.

(15) Jani, J. M.; Leary, M.; Subic, A.; Gibson, M. A. A Review of Shape Memory Alloy Research, Applications and Opportunities. *Mater. Eng.* **2014**, *56*, 1078–1113.

(16) Wang, W.; Kim, N.-G.; Rodrigue, H.; Ahn, S.-H. Modular Assembly of Soft Deployable Structures and Robots. *Mater. Horiz.* **2017**, *4*, 367–376.

(17) Laschi, C.; Mazzolai, B.; Cianchetti, M. Soft Robotics: Technologies and Systems Pushing the Boundaries of Robot Abilities. *Science Robotics* **2016**, *1*, eaah3690.

(18) Mantovani, D. Shape Memory Alloys: Properties and Biomedical Applications. *JOM* **2000**, *52*, 36–44.

(19) Kauffman, G. B.; Mayo, I. Memory Metal. *ChemMatters* **1993**, 4–7.

(20) Petrini, L.; Migliavacca, F. Biomedical Applications of Shape Memory Alloys. *J. Metall. (N. Y., NY, U. S.)* **2011**, *2011*, 501483.

(21) Frenzel, J.; George, E. P.; Dlouhy, A.; Somsen, C.; Wagner, M. F.-X.; Eggeler, G. Influence of Ni on Martensitic Phase Transformations in NiTi Shape Memory Alloys. *Acta Mater.* **2010**, *58*, 3444–3458.

(22) Song, C. History and Current Situation of Shape Memory Alloys Devices for Minimally Invasive Surgery. *Open Medical Devices Journal* **2010**, *2*, 24–31.

(23) Miyazato, M.; Yoshimura, N.; Chancellor, M. B. The Other Bladder Syndrome: Underactive Bladder. *Rev. Urol.* **2013**, *15*, 11–22.

(24) Yoshida, M.; Yamaguchi, O. Detrusor Underactivity: The Current Concept of the Pathophysiology. *LUTS: Lower Urinary Tract Symptoms* **2014**, *6*, 131–137.

(25) Gammie, A.; Kaper, M.; Dorrepaal, C.; Kos, T.; Abrams, P. Signs and Symptoms of Detrusor Underactivity: An Analysis of Clinical Presentation and Urodynamic Tests from a Large Group of Patients Undergoing Pressure Flow Studies. *Eur. Urol.* **2016**, *69*, 361–369.

(26) Chancellor, M. B. Epidemiology and Demographics of Underactive Bladder. In *The Underactive Bladder*; Chancellor, M. B., Diokno, A. C., Eds.; Springer International Publishing: Switzerland, 2016; pp 1–11.

(27) Hoag, N.; Gani, J. Underactive Bladder: Clinical Features, Urodynamic Parameters, and Treatment. *International Neurouroly Journal* **2015**, *19*, 185–189.

(28) Wyndaele, J. J. Intermittent Catheterization: Which is the Optimal Technique? *Spinal Cord* **2002**, *40*, 432–437.

(29) Hooton, T. M.; Bradley, S. F.; Cardenas, D. D.; Colgan, R.; Geerlings, S. E.; Rice, J. C.; Saint, S.; Schaeffer, A. J.; Tambayh, P. A.; Tenke, P.; Nicolle, L. E. Diagnosis, Prevention, and Treatment of Catheter Associated Urinary Tract Infection in Adults: 2009

International Clinical Practice Guidelines from the Infectious Diseases Society of America. *Clin. Infect. Dis.* **2010**, *50*, 625−663.

(30) Ramakrishnan, K.; Mold, J. Urinary Catheters: A Review. *Internet J. Fam. Pract.* **2004**, *3*, 1−12.

(31) Wyndaele, J. J. Complications of Intermittent Catheterization: Their Prevention and Treatment. *Spinal Cord* **2002**, *40*, 536−541.

(32) Hassani, F. A.; Peh, W. Y. X.; Gammad, G. G. L.; Mogan, R. P.; Ng, T. K.; Kuo, T. L. C.; Ng, L. G.; Luu, P.; Yen, S.-C.; Lee, C. A 3D Printed Implantable Device for Voiding the Bladder Using Shape Memory Alloy (SMA) Actuators. *Adv. Sci. (Weinheim, Ger.)* **2017**, *4*, 1700143.

(33) Hassani, F. A.; Gammad, G. G. L.; Mogan, R. P.; Ng, T. K.; Kuo, T. L. C.; Ng, L. G.; Luu, P.; Thakor, N. V.; Yen, S.-C.; Lee, C. Design and Anchorage Dependence of Shape Memory Alloy Actuators on Enhanced Voiding of a Bladder. *Adv. Mater. Technol. (Weinheim, Ger.)* **2018**, *3*, 1700184.

(34) Liao, W.-C.; Jaw, F.-S. Noninvasive Electrical Impedance Analysis to Measure Human Urinary Bladder Volume. *J. Obstet. Gynaecol. Res.* **2011**, *37*, 1071−1075.

(35) Merks, E. J. W. *Instantaneous Ultrasonic Assessment of Urinary Bladder*. Ph.D. Thesis, Erasmus University Rotterdam, Netherlands, June 2009.

(36) Selius, B. A.; Subedi, R. Urinary Retention in Adults: Diagnosis and Initial Management. *Am. Fam. Physician* **2008**, *77*, 643−650.

(37) Tam, C. K.; Wong, K. K.; Yip, W. M. Prevalence of Incomplete Bladder Emptying Among Elderly in Convalescent Wards: A Pilot Study. *Asian J. Gerontol. Geriatr.* **2006**, *2*, 66−71.

(38) Udoh, E. A.; Eyo, A. E. Pattern of Urine Volume Drained after Catheterization for Urinary Retention. *SAS J. Med.* **2016**, *2*, 147−151.

(39) Barth, J.; Kohl, M. A Bistable Magnetically Enhanced Shape Memory Microactuator with High Blocking Forces. *Phys. Procedia* **2010**, *10*, 189−196.

(40) Wu, S.-Y.; Jhang, J.-F.; Jiang, Y.-H.; Kuo, H.-C. Increased Bladder Wall Thickness is Associated with Severe Symptoms and Reduced Bladder Capacity in Patients with Bladder Pain Syndrome. *Urol. Sci.* **2016**, *27*, 263−268.

(41) Yoda, R. Elastomers for Biomedical Applications. *J. Biomater. Sci., Polym. Ed.* **1998**, *9*, 561−626.

(42) Hill, W. G. Control of Urinary Drainage and Voiding. *Clin. J. Am. Soc. Nephrol.* **2015**, *10*, 480−492.

(43) Dagdeviren, C.; Yang, B. D.; Su, Y.; Tran, P. L.; Joe, P.; Anderson, E.; Xia, J.; Doraiswamy, V.; Dehdashti, B.; Feng, X.; Lu, B.; Poston, R.; Khalpey, Z.; Ghaffari, R.; Huang, Y.; Slepian, M. J.; Rogers, J. A. Conformal Piezoelectric Energy Harvesting and Storage from Motions of the Heart, Lung, and Diaphragm. *Proc. Natl. Acad. Sci. U. S. A.* **2014**, *111*, 1927−1932.

(44) Li, J.; Wang, X. Research Update: Materials Design of Implantable Nanogenerators for Biomechanical Energy Harvesting. *APL Mater.* **2017**, *5*, 073801.

(45) Zheng, Q.; Zhang, H.; Shi, B.; Xue, X.; Liu, Z.; Jin, Y.; Ma, Y.; Zou, Y.; Wang, X.; An, Z.; Tang, W.; Zhang, W.; Yang, F.; Liu, Y.; Lang, X.; Xu, Z.; Li, Z.; Wang, Z. L. *In Vivo* Self-Powered Wireless Cardiac Monitoring *via* Implantable Triboelectric Nanogenerator. *ACS Nano* **2016**, *10*, 6510−6518.

(46) Li, Z.; Zhu, G.; Yang, R.; Wang, A. C.; Wang, Z. L. Muscle-Driven *In Vivo* Nanogenerator. *Adv. Mater. (Weinheim, Ger.)* **2010**, *22*, 2534−2537.

(47) Wang, Z. L. Triboelectric Nanogenerators as New Energy Technology and Self-Powered Sensors− Principles, Problems and Perspectives. *Faraday Discuss.* **2014**, *176*, 447−458.

(48) Lee, S.; Wang, H.; Shi, Q.; Dhakar, L.; Wang, J.; Thakor, N. V.; Yen, S.-C.; Lee, C. Development of Battery-Free Neural Interface and Modulated Control of Tibialis Anterior Muscle *via* Common Peroneal Nerve Based on Triboelectric Nanogenerators (TENGs). *Nano Energy* **2017**, *33*, 1−11.

(49) Feng, H.; Zhao, C.; Tan, P.; Liu, R.; Chen, X.; Li, Z. Nanogenerator for Biomedical Applications. *Adv. Healthcare Mater.* **2018**, 1701298.

(50) Kellogg's Research Lab, *Nitinol Springs*. https://www.kelloggsresearchlabs.com/Nitinol/Nitinol-springs (accessed March 7, 2018).

(51) DYNALLOY, Inc. *Technical Characteristics of FLEXINOL Actuator Wires*. www.dynalloy.com/pdfs/TCF1140.pdf (accessed March 7, 2018).

(52) Shimoseki, M. Role of FEM in Spring Analysis. In *FEM for Springs*; Shimoseki, M., Hamano, T., Imaizumi, T., Eds.; Springer-Verlag: Germany, 2003; pp 53−66.

(53) Mehrpouya, M.; Shahedin, A. M.; Dawood, S. D. S.; Ariffin, A. K. An Investigation on the Optimum Machinability of NiTi Based Shape Memory Alloy. *Mater. Manuf. Processes* **2017**, *32*, 1497−1504.

(54) Fedder, G. K. System-Level Simulation of Microsystems. In *MEMS: A Practical Guide of Design, Analysis and Applications*; Korvink, J. G., Paul, O., Eds.; William Andrew: New York, 2006; pp 187−227.

(55) Ashby, M. F. Materials Selection − The Basics. In *Materials Selection in Mechanical Design*; Butterworth-Heinmann: United Kingdom, 1999; pp 65−84.

(56) Cambridge University, Engineering Department, *Materials Data Book*, 2003. http://www-mdp.eng.cam.ac.uk/web/library/enginfo/cueddatabooks/materials.pdf (accessed March 7, 2018).

(57) Li, C.; Guan, G.; Zhang, F.; Song, S.; Wang, R. K.; Huang, Z.; Nabi, G. Quantitative Elasticity Measurement of Urinary Bladder Wall Using Laser-Induced Surface Acoustic Waves. *Biomed. Opt. Express* **2014**, *5*, 4313−4328.

(58) DeWachter, S.; De Laet, K.; Wyndaele, J. J. Does the Cystometric Filling Rate Affect the Afferent Bladder Response Pattern? A Study on Single Fibre Pelvic Nerve Afferents in the Rat Urinary Bladder. *Neurourol. Urodyn.* **2006**, *25*, 162−167.

(59) Bluvshtein, V.; Lucke, L. Safe Wireless Power Design for Implanted Medical Devices. *J. Med. Devices* **2014**, *8*, 020916.

(60) Yuan, Z.; Zhou, T.; Yin, Y.; Cao, R.; Li, C.; Wang, Z. L. Transparent and Flexible Triboelectric Sensing Array for Touch Security Applications. *ACS Nano* **2017**, *11*, 8364−8369.

(61) Lin, Z.; Chen, J.; Li, X.; Zhou, Z.; Meng, K.; Wei, W.; Yang, J.; Wang, Z. L. Triboelectric Nanogenerator Enabled Body Sensor Network for Self-Powered Human Heart-Rate Monitoring. *ACS Nano* **2017**, *11*, 8830−8837.

(62) Hassani, F. A.; Lee, C. A Triboelectric Energy Harvester Using Low Cost, Flexible and Biocompatible Ethylene Vinyl Acetate (EVA). *J. Microelectromech. Syst.* **2015**, *24*, 1338−1345.

(63) Shi, Q.; Wu, H.; Wang, H.; Wu, H.; Lee, C. Self-Powered Gyroscope Ball Using Triboelectric Mechanism. *Adv. Energy Mater.* **2017**, *7*, 1701300.

(64) Wang, H.; Wu, H.; Hasan, D.; He, T.; Shi, Q.; Lee, C. Self-Powered Dual-Mode Amenity Sensor Based on the Water−Air Triboelectric Nanogenerator. *ACS Nano* **2017**, *11*, 10337−10346.

(65) Object, *FullCure Materials*. http://svl.wpi.edu/wp-content/uploads/2014/04/FullCure_Letter_low-1.pdf (accessed March 7, 2018).

DOI: 10.1021/acsnano.8b00303
ACS Nano 2018, 12, 3487−3501